Available online at www.sciencedirect.com
SCIENCE DIRECT®
Nuclear Instruments and Methods in Physics Research A 557 (2006) 436–444
NUCLEAR INSTRUMENTS & METHODS IN PHYSICS RESEARCH Section A
www.elsevier.com/locate/nima

# A beam test of a prototype of the BESIII drift chamber in magnetic field

J.B. Liu[a,*], Z.H. Qin[a,b], L.H. Wu[a,b], C. Chen[a], B.A. Zhuang[a], Y.B. Chen[a], Y. Jin[a], R.G. Liu[a], X.Y. Ma[a], Y.Y. Ma[a], X. Tang[a], L. Wang[a], M.H. Xu[a], G.F. Zhang[a], M.X. Zhu[a], Q.M. Zhu[a]

[a]*Institute of High Energy Physics, Chinese Academy of Sciences, Beijing 100049, China*
[b]*Graduate School of the Chinese Academy of Sciences, Beijing 100049, China*

Received 11 November 2005; accepted 11 November 2005
Available online 5 December 2005

**Abstract**

A prototype of the BESIII drift chamber was tested with $He/C_3H_8(60/40)$ gas mixture in a 1T magnetic field at the π-2 beam line of KEK 12 GeV PS. The drift distance–time relationship was extracted for various conditions. The performance of the chamber, such as the spatial resolution, the $dE/dx$ resolution and the cell efficiency, was studied in detail. The $dE/dx$ was measured as a function of $\beta\gamma$ to calculate the particle separation power. Based on the test results, the operating voltage of the BESIII drift chamber is optimized to be 2200 V, resulting in a spatial resolution better than 110 μm, a cell efficiency over 98%, a $dE/dx$ resolution better than 5% and the $3\sigma$ π/K separation at a momentum exceeding 700 MeV/$c$. These results confirm the validation of the physics design of the BESIII drift chamber.


*PACS:* 29.40.Gx

*Keywords:* BESIII; Drift chamber; Beam test; Resolution

## 1. Introduction

The BESIII experiment [1] at the upgrading Beijing Electron Positron Collider (BEPCII, $L\sim10^{33}\,cm^{-2}\,s^{-1}$@ $E_{cm}=3.78$ GeV) [2] is designed for high-precision measurements and new physics searches in the τ-charm energy region. Such goals require that exclusive final states from the $e^+e^-$ collision be reconstructed efficiently and with high resolution. This makes stringent demands on the performance of the central tracking chamber. The BESIII central tracking chamber, located in a 1T magnetic field, must provide maximal solid angle coverage, good momentum resolution in a range of 0.1–2 GeV/$c$, and efficient tracking down to 50 MeV/$c$. In addition, the tracking chamber is expected to provide one of the principal triggers and the particle identification for low momentum charged particles through $dE/dx$ measurements. Finally, the chamber must be operational with stability and safety at the expected background of the BEPCII, estimated to be about 50 kHz/cell for the innermost layer [1]. In order to meet the above requirements, the BESIII tracking chamber is designed to be a small-cell, low-mass drift chamber operated using a helium-based gas mixture, with a spatial resolution better than 130 μm averaged over the cell, a $dE/dx$ resolution better than 6% for π/K separation up to a momentum of 700 MeV/$c$, and a transverse momentum resolution of about 0.5%@1 GeV/$c$.

The BESIII drift chamber adopts the drift cell with almost square shape. All the cells are arranged in 43 circular layers. The radial extent is from 73 to 771 mm occupied successively by 8 stereo layers, 12 axial layers, 16 stereo layers and 7 axial layers. Each layer contains a field wire layer (with all field wires) and a sense wire layer (with alternating sense and field wires). The space between sense and field layers is carefully adjusted to minimize the asymmetry in the drift distance–time relation ($x$–$t$ relation) on the left and right sides of each cell in the magnetic field [3]. The cell size is about $12\times12\,mm^2$ for the 8 inner layers, in order to have high granularity and less aging effect, and about $16.2\times16.2\,mm^2$ for the following 35 layers. The working gas of the chamber is chosen to be

*Corresponding author. Tel.: +86 10 88236069; fax: +86 10 88236423.
*E-mail address:* liujb@ihep.ac.cn (J.B. Liu).

0168-9002/$ - see front matter © 2005 Elsevier B.V. All rights reserved.
doi:10.1016/j.nima.2005.11.093

$He/C_3H_8(60/40)$, together with the use of other low-mass materials, such as aluminum field wires and carbon fiber inner and outer cylindrical walls, so as to minimize the effect of multiple scattering. The detailed information about the chamber's design can be found in Ref. [1].

In order to verify the physics design of the BESIII drift chamber accurately and optimize the operating voltage, a prototype of the chamber was built and a beam test was performed with the gas mixture of $He/C_3H_8(60/40)$ in a 1T magnetic field at the π-2 beam line of KEK 12 GeV PS. In the following sections, the prototype, the beam test layout, the electronics and data acquisition system are described. The test results, including the $x$–$t$ relation, the spatial resolution, the $dE/dx$ measurement, the cell efficiency, are presented and discussed in detail. The conclusion is given at the last.

## 2. Experimental setup

### 2.1. The prototype of the BESIII drift chamber

The prototype consists of 78 drift cells, arranged in 12 layers of 6–9 cells to model a small section of a cylindrical chamber structure, as shown in Fig. 1. Each cell, in almost squared shape, has one sense wire surrounded by a grid of eight field wires which are shared by adjacent cells. The wires are the same type for the BESIII drift chamber: 25 μm diameter gold-plated tungsten (3% Re) sense wires and 110 μm diameter gold-plated aluminum field wires. The outer seven layers reproduce a small section of the outermost seven axial layers of the BESIII drift chamber, while the inner five layers are arranged by transferring a small section of the innermost five stereo layers at one end of the drift chamber to the position with the large radius. All the layers are axial. The average half-cell size is about 6 mm for Layers 1–5 and about 8.1 mm for Layers 6–12. The gap between Layers 5 and 6 in the prototype is set to study the impact of the axial–stereo boundaries in the BESIII drift chamber.

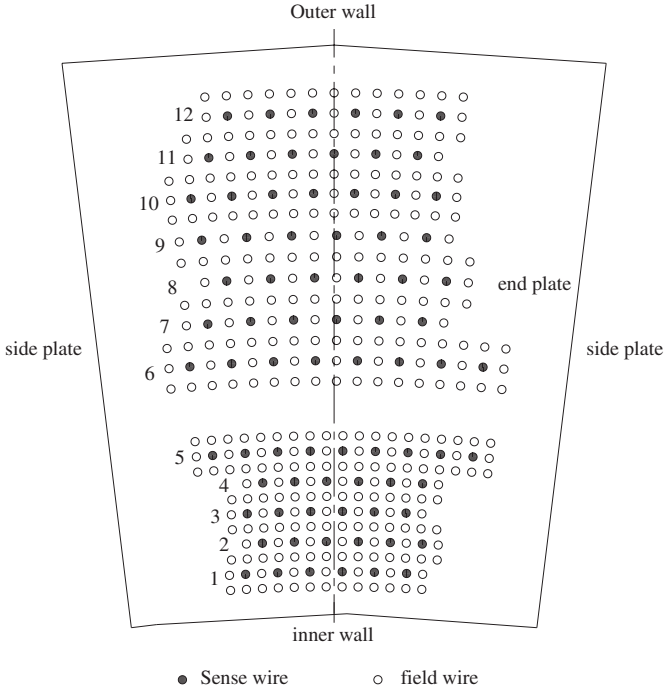


Fig. 1. Layout and structure of the prototype. The figure on the left of each layer indicates the layer number.

The prototype has a shape of a cylindrical sector, with inner radius of 57 cm and outer radius of 79 cm. Because of the limited aperture size of the magnet, the length of the prototype is restricted to be 30 cm and the length of wires is about 20 cm. The mechanical structure of the prototype, all made of aluminum, is composed of two end plates, two side plates, and inner and outer walls. The inner and outer walls are in arc shape to reproduce the impact of the cylindrical inner and outer walls in the BESIII Drift chamber. The walls are only 0.6 mm thick to reduce the multiple scattering of the beam particles.

Six preamplifier boards, each with eight channels, were mounted on the two side plates to save the longitudinal space. Only the four central cells in each layer were read out. The positive high voltage was supplied to all sense wires at one end plate to correctly shape the electric field in the central cells. The voltage applied to each sense layer was tuned to provide the same gas gain, and all the voltages are collectively represented by a reference voltage applied to the $16.2 \times 16.2\,mm^2$ cell. The field wires were at ground potential, except those at boundaries where positive compensating voltages of 100–200 V were applied to reduce the large left–right asymmetry of the $x$–$t$ relations of the boundary layers (Layers 1, 5, 6, 12) in a magnetic field.

### 2.2. Beam test layout

The beam test was performed at the $\pi - 2$ beam line of the KEK 12 GeV Proton Synchrotron. The test layout is shown in Fig. 2. The beam contains proton, $\pi^+$, when the beam polarity is positive, and electron, $\pi^-$, for negative beam polarity, with a momentum range from 0.6 to 4 GeV/$c$. Two pairs of scintillation counters (SC1–SC4) were placed 9 m apart along the beam line to provide the event trigger by four-fold coincidence and the time-of-fight measurement for the separation of proton and $\pi^+$ in the whole momentum range. Two threshold Cherenkov counters (C1 and C2) filled with $CO_2$ lied between the two pairs of scintillation counters to provide electron identification up to 3 GeV/$c$. C1 and C2 were also part of the electron event trigger to improve the efficiency of the data taking. A magnet with the useful aperture size of $80(\text{width}) \times 60(\text{length}) \times 30(\text{height})\,cm^3$ was available on the beam line downstream. The magnetic field in vertical direction can be adjusted in the range from 0 to 2 T. The prototype was placed inside the aperture of the magnet with wires parallel to the magnetic field in order to study the chamber performance in a 1T magnetic field. Behind the magnet there were two lead glass counters (LG1 and

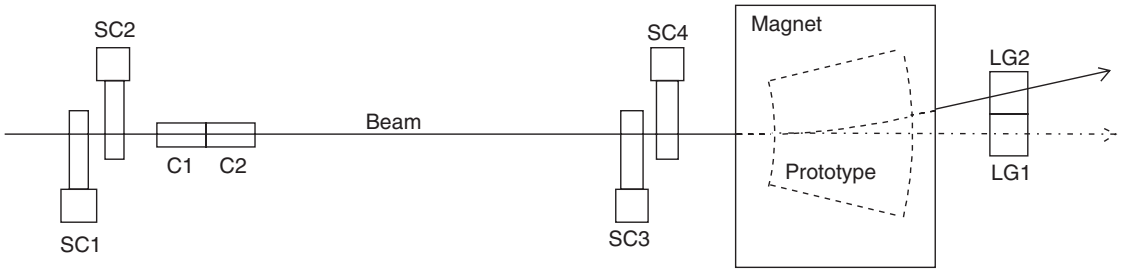


Fig. 2. The beam test layout.

LG2) used to identify electrons at all the momentum by the energy deposition. In addition, these two counters can be used to suppress $\pi^+$ backgrounds in order to select low momentum ($<1\,\mathrm{GeV}/c$) protons since the $\pi^+$ produce signals in the lead glass counter while proton do not.

A gas mixture of $He/C_3H_8(60/40)$ was supplied by mass flow meters at a rate of 1 volume/h with a pressure controlled by bubbling the output gas through $\sim$1 cm of silicon oil.

### 2.3. Electronics and data acquisition

The trigger signal is delayed and fanned out to TDC (LRS2229) as the start signal and to ADC (LRS2249W) as the gate signal. The sense wire signal is amplified by the trans-impedance type of preamplifier with a gain of 12 kΩ and a rise time of 5 ns, designed for the BESIII drift chamber. The signal from the preamplifier is sent to the main amplifier, which split the signal into two. One is amplified and discriminated, then fed to TDC as the stop signal for the drift time measurement. The other one is shaped and amplified, fed to ADC for the charge measurement. The width of the ADC gate is set to be 800 ns, corresponding to the maximum drift time plus the signal width. The data are read out by a PC through the CAMAC bus. In addition, a special calibration circuit composed of a controller, a pulse generator and a pulse distributor is used to calibrate the system.

## 3. Results

### 3.1. x–t relation

The prototype chamber is self-tracking, so an iterative algorithm is used to extract the $x$–$t$ relation starting from a rough one as the seed. A track is fitted first to circles centered at the sense wires of hit cells with the radii equal to the drift distance which is calculated from the measured drift time using the $x$–$t$ relation. The average residuals of the fitted track to the drift distance for each drift time bin are then used to correct the $x$–$t$ relation to obtain a new one. The process is iterated several times until the $x$–$t$ relation is converged. In order to avoid bias, the cell used for the calculation of residuals is excluded from the track fitting. Different $x$–$t$ relations are obtained for each layer and for the left and right sides of cells. The time offset and the wire position are adjusted channel by channel so that the residual distributions on the left and right sides of each cell center at about zero.

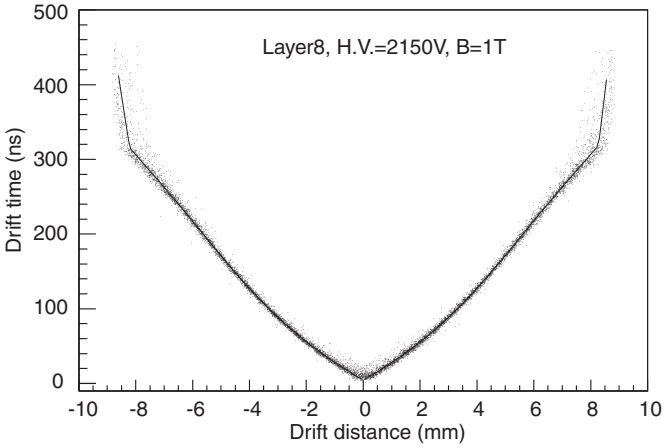


Fig. 3. Typical $x$–$t$ scatter plot.

Fig. 3 shows a typical $x$–$t$ scatter plot. The $x$–$t$ relation is smooth in a large portion of the cell except near the edge where it is distorted, which is mainly due to the distorted electric field near the field wires. The $x$–$t$ relation is fitted to a fifth order polynomial in the smooth region plus first order polynomial near the edge, as shown in Fig. 3. The drift time at the conjunction of the two polynomial is chosen to be the midpoint of the falling edge of the drift time distribution. The nonlinear behavior of the $x$–$t$ relation is a significant character of the small cell drift chamber caused by the non-uniform electric field due to its cell geometry.

The magnetic field changes the amplitude and the direction of the drift velocity of electrons. Its impact on the $x$–$t$ relation in a 1T magnetic field is shown in Fig. 4. The drift time in magnetic field increases, especially in the region far from the sense wire, mainly due to the change of the drift path of electrons. Electrons drift in a magnetic field not along the electric field, but with a Lorentz angle, causing a curved and longer drift path. The largest drift time difference between $B=0$ and 1T, at a far drift distance, observed in Fig. 4, is about 40 ns, and the maximum drift time in the 1T magnetic field is about 320 ns, acceptable for BEPCII.

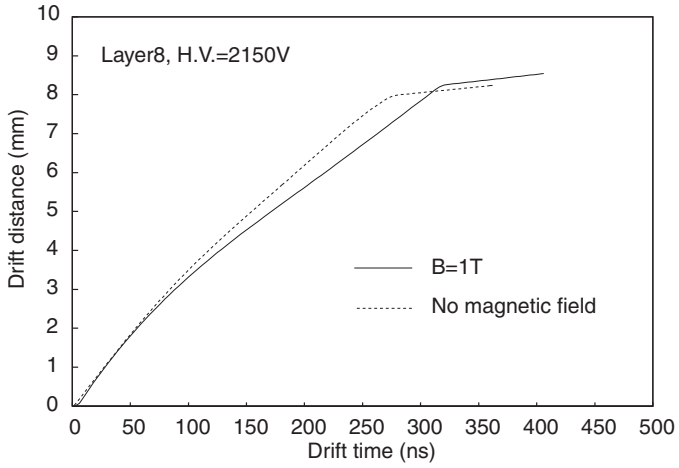


Fig. 4. $x$–$t$ relations at $B = 0$ and 1T.

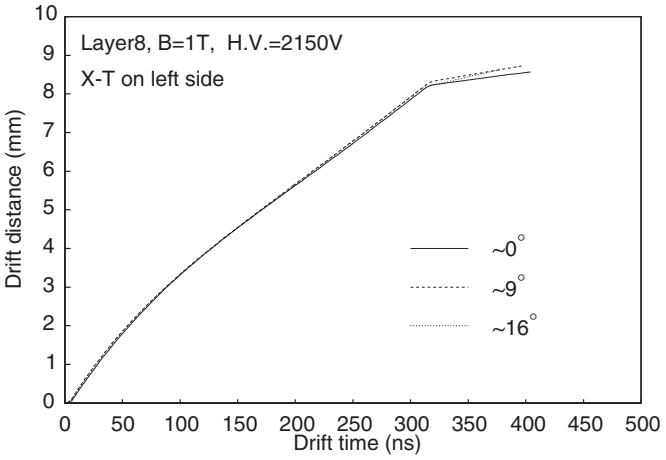


Fig. 6. $x$–$t$ relations for different incident angles.

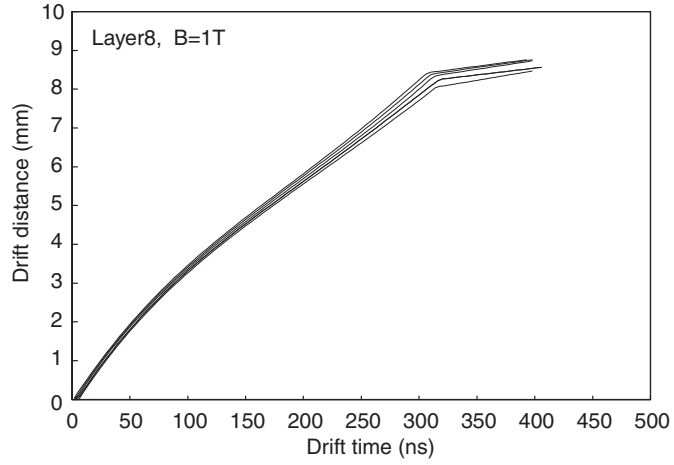


Fig. 5. $x$–$t$ relations for various operating voltages. From the bottom to the top, the applied voltages are 2100, 2150, 2200, 2250 and 2300 V, respectively.

Since the electric field in the small cell is not uniform and the helium-based working gas is not saturated in a large portion of the cell, the operating voltage has a large impact on the $x$–$t$ relation as shown in Fig. 5. There exists a large difference for $x$–$t$ relations at different operating voltages, and the impact is more evident in the region far from the sense wire where the electric field is relatively low.

Fig. 6 shows the $x$–$t$ relations at different incident angles (the angle between the track and the cell radial direction in the transverse plane). The dependence is very small, up to about 16°, due to the square shape of the cell which produces a comparatively isotropic electric field. Such a phenomena will simplify the calibration for the BESIII drift chamber.

As described in Section 2.1, the boundary field layers were applied with compensating voltages to reduce the large left–right asymmetry of the $x$–$t$ relations in a magnetic field, as shown in Fig. 7. The largest drift time difference between the left and right sides at a given distance from the sense wire is greater than 20 ns before the compensation, and can be reduced to be within 1 ns after the compensation. The $x$–$t$ left–right asymmetry arises from the radial asymmetry of the electric field of a cell since the boundary condition greatly enhances the electric field. Applying positive compensation voltage on the boundary field layers can reduce the electric field on the boundary efficiently so as to reduce the $x$–$t$ left–right asymmetry. The left–right symmetry of the $x$–$t$ relation can simplify calibration procedures and result in smaller corrections.

### 3.2. Spatial resolution

The spatial resolution is determined from the residual distribution after the track fitting using the final $x$–$t$ relation, where the track fit error has been subtracted from the residual using the technique described in Ref. [4]. Fig. 8 shows a typical residual distribution of all layers, which has a non-Gaussian tail, mainly caused by the non-isochronic charge collection in the drift cell, i.e. electrons from the primary ionization arriving to the sense wire not at the same time. This is a major limiting factor to the spatial resolution of a small cell. The dual Gaussian is used to fit the residual distribution and the resolution is calculated using the formula as shown in Fig. 8.

The average spatial resolution in each layer is shown in Fig. 9 in a 1T magnetic field, together with that without the magnetic field for comparison. The magnetic field might deteriorate the spatial resolution due to the Lorentz angle effect which enhances the non-isochronic charge collection. However, due to the small Lorentz angle of $He/C_3H_8(60/40)$, it is seen from the plot that the magnetic field has a very small impact on the spatial resolution except for the boundary layers. The spatial resolutions of the boundary layers are worse than those of other layers, showing the effect of the boundary in the drift chamber.

Fig. 10 shows the drift distance dependent spatial resolution which deteriorates near the sense wire due to the statistics of primary ionization coupled to the

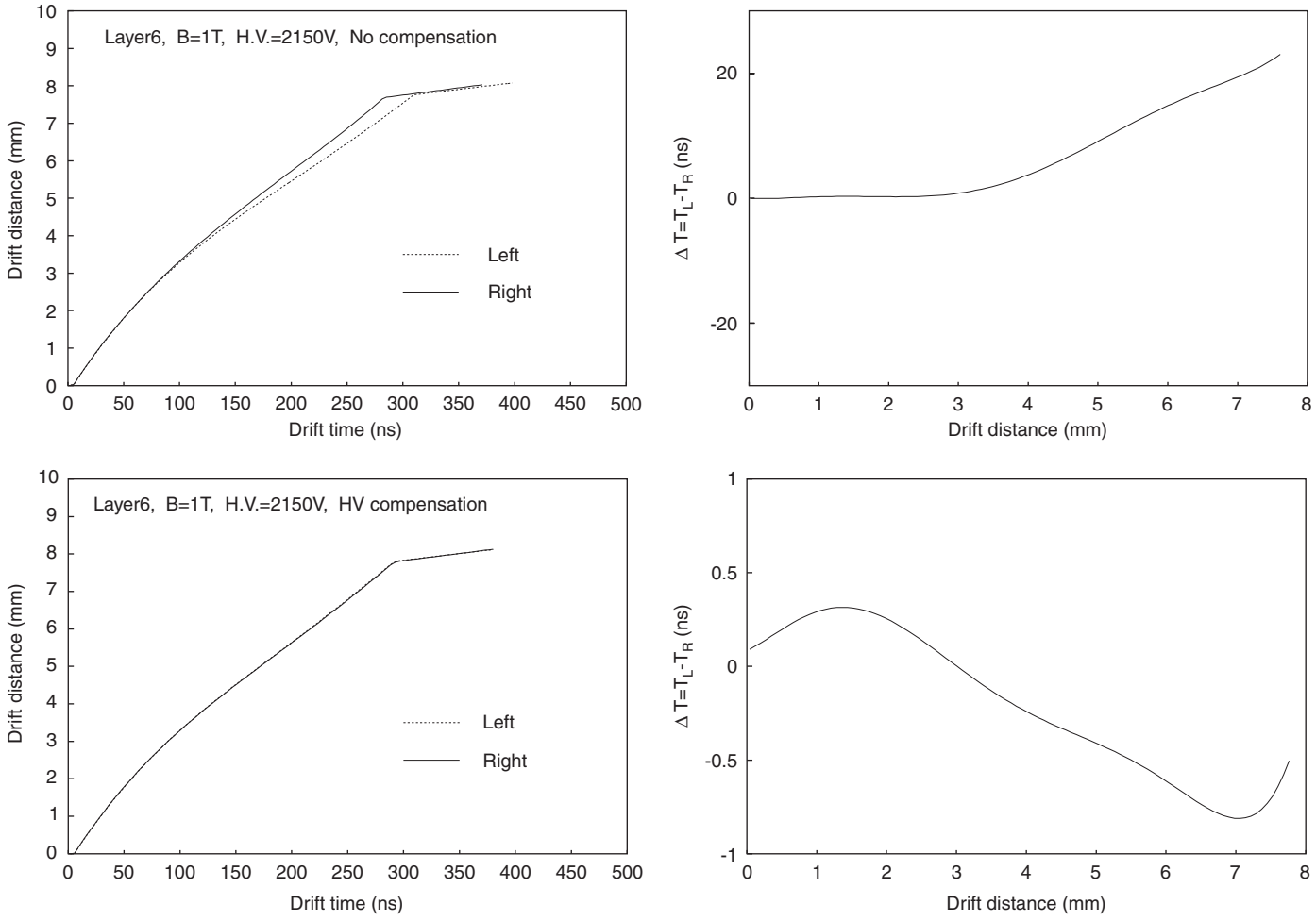


Fig. 7. The impact of the compensation voltage on the boundary layer $x$–$t$ relation. The left shows the $x$–$t$ relations on the left and right sides of one cell, while the right shows the left–right differences of the drift time as a function of the drift distance.

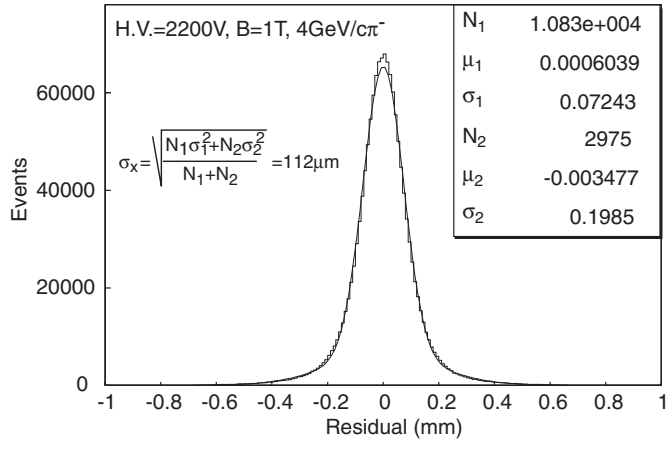


Fig. 8. Typical residual distribution.

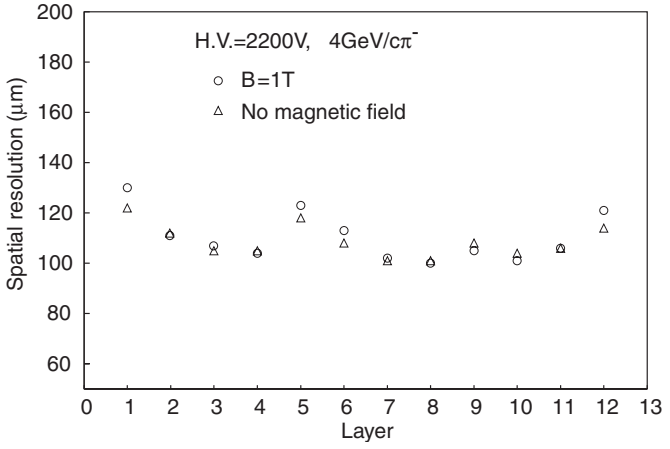


Fig. 9. Spatial resolutions for all layers.

non-isochronic charge collection caused by the radial electric field near the sense wire. The sharp degradation of the spatial resolution near the cell edge is due to the distortion of the electric field which results in serious non-isochronic behavior.

The average spatial resolution of the prototype in a 1T magnetic field, excluding boundary layers, is shown in Fig. 11 as a function of the operating voltage. Increasing the operating voltage results in larger signal amplitude, hence smaller time-walk effect and better spatial

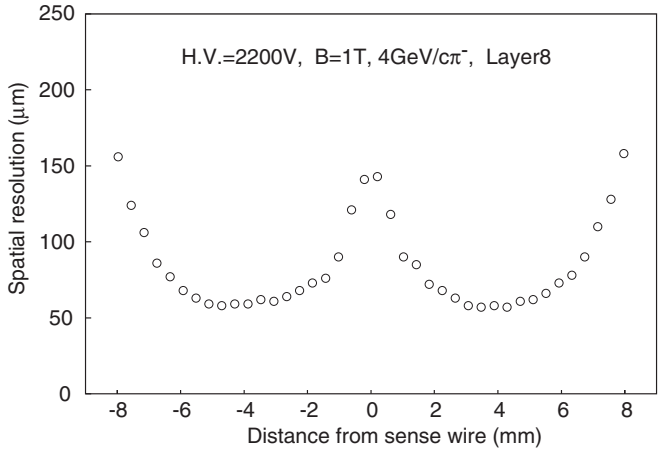


Fig. 10. Dependence of the spatial resolution on the drift distance.

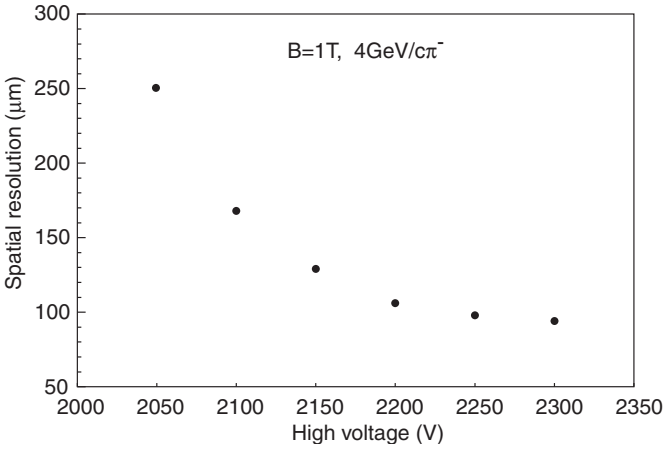


Fig. 11. Spatial resolution as a function of the operating voltage.

resolution. However, if the voltage exceeds 2200 V, the improvement is very limited and the resolution is better than 110 μm for 2200 V, and close to 90 μm for 2300 V. Such a result indicates that the BESIII drift chamber can obtain a good spatial resolution in a strong magnetic field of 1T.

### 3.3. $dE/dx$ measurement

The $dE/dx$ measurements are performed using layers with large cell size (Layers 6–12), since the majority of layers in the BESIII drift chamber (35 out of 43 layers) have the similar size. The $dE/dx$ is measured by using its truncated mean [5] to reduce the effect of the Landau tail, hence a Landau spectrum of $dE/dx$ is converted into a Gaussian-like spectrum. In order to perform the

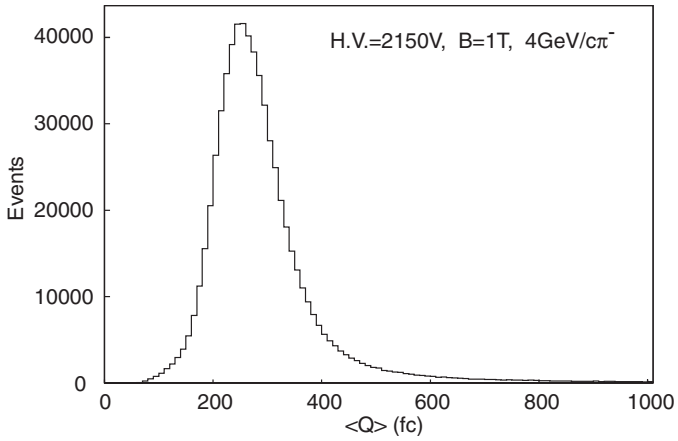


Fig. 13. Charge distribution from a single cell.

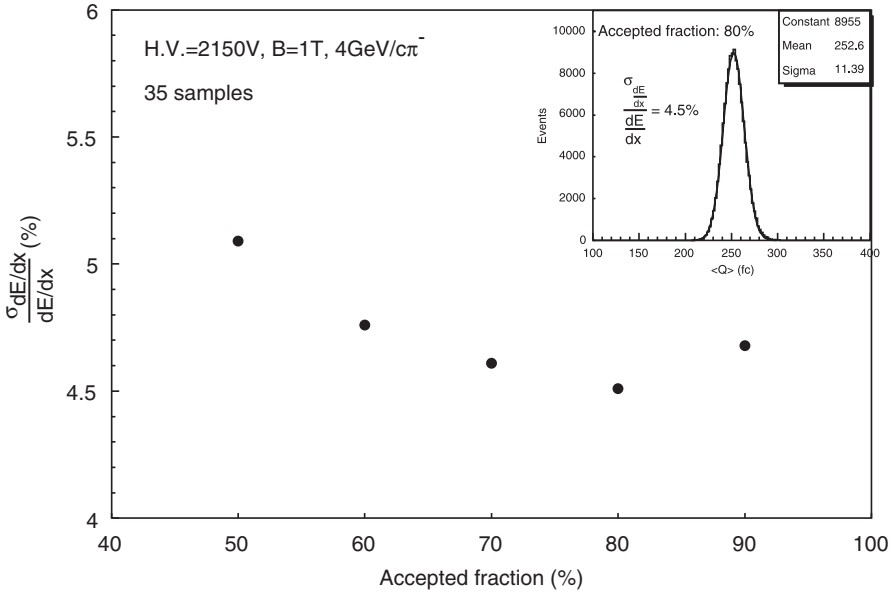


Fig. 12. $dE/dx$ resolution as a function of the accepted fraction. Shown in the inset is the Gaussian-like truncated mean spectrum at the accepted fraction of 80%.

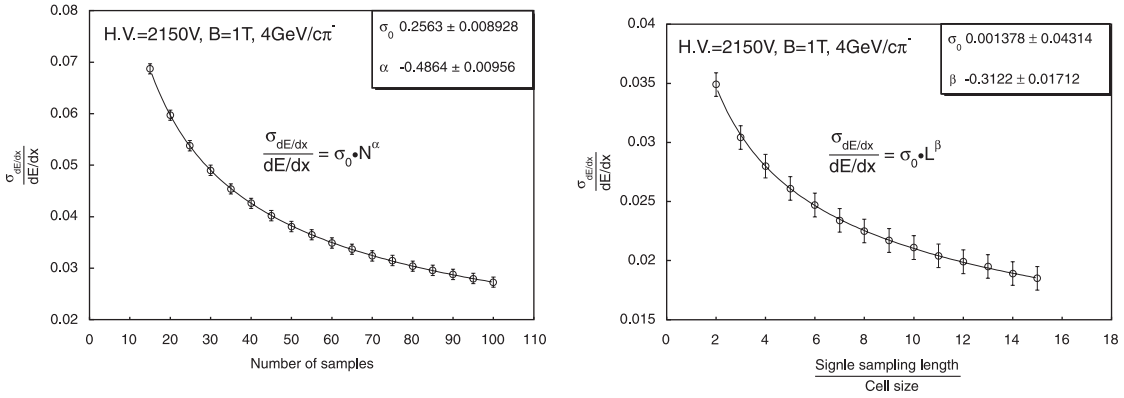


Fig. 14. Dependence of the $dE/dx$ resolution on the number of samples (left) and the sampling length (right).

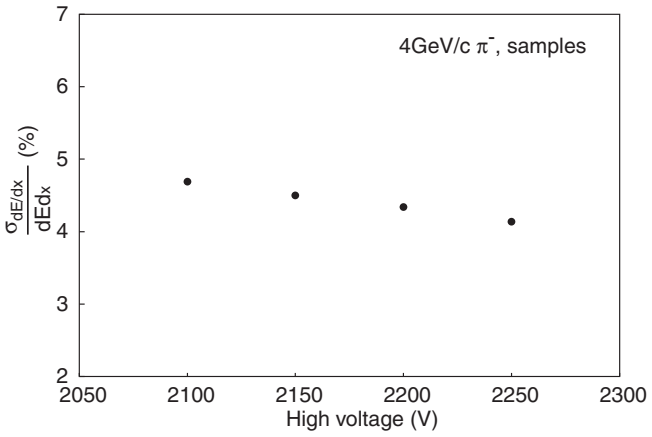


Fig. 15. $dE/dx$ resolution at different operating voltages.

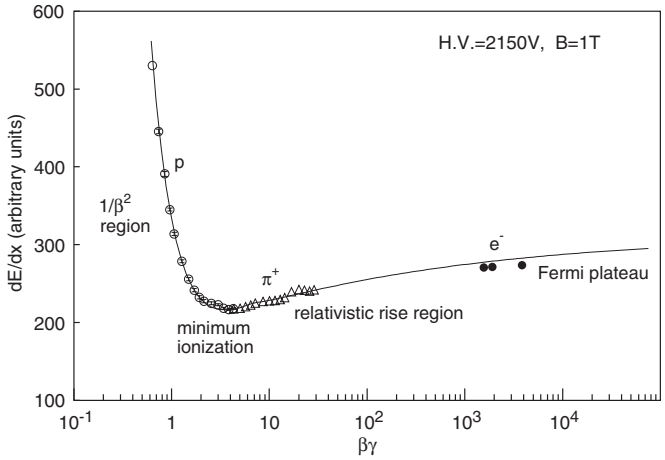


Fig. 16. Measured $dE/dx$ vs. $\beta\gamma$.

measurement with the desired number of samples, the hits from different events are combined to form fake tracks.

The best $dE/dx$ resolution is obtained by averaging the 80% lowest $dE/dx$ values as shown in Fig. 12. For a fraction higher than 80%, the resolution becomes worse due to the inclusion of hits from the Landau tail, while for a smaller fraction the loss in statistics worsens the resolution. The relatively large accepted fraction of 80%, as compared with argon-based gas mixtures, is due to the reduced Landau tail in $He/C_3H_8(60/40)$ as shown in Fig. 13.

The $dE/dx$ resolution depends on the number of samples and the length of each sampling. Fig. 14 shows the results, where the large sampling length is simulated by summing up the pulse heights of hit cells in different layers. The solid curve is a fit using the following parameterized formula [6]:

$$\frac{\sigma_{dE/dx}}{dE/dx} \propto N^{\alpha} \cdot l^{\beta}$$

where $N$ is the number of samples, $l$ is the length of sampling and $\alpha, \beta$ are the parameters, which are fit to be $\alpha = -0.486 \pm 0.010$ and $\beta = -0.312 \pm 0.017$. In the case of the BESIII drift chamber(30–40 samples), a $dE/dx$ resolution of better than 5% can be obtained from this formula. The improvement of the $dE/dx$ resolution with the increase of the number of samples is smaller than $N^{-0.5}$ as expected from a simple Gaussian. The fact that $\alpha$ value is very close to $-0.5$ confirms that the Landau tail in $He/C_3H_8(60/40)$ is small. On the other hand, the $\alpha$ value is less than the $\beta$ value. It indicates that the contribution of the number of samples to the $dE/dx$ resolution is larger than that of the sampling length. It should be pointed out that using sum of hit cells to simulate the large sampling length might be different from the real case.

The $dE/dx$ resolution at different operating voltages is shown in Fig. 15. The higher voltage produces the larger pulse height, hence increases the signal-to-noise ratio resulting in a better $dE/dx$ resolution.

The dependence of $dE/dx$ on $\beta\gamma$ was measured as shown in Fig. 16, where the $dE/dx$ was measured as the truncated mean with 35 samples and the accepted fraction of 80%. The solid curve in the figure is a fit using the restricted energy loss formula [7]:

$$\frac{dE}{dx} \propto \frac{1}{\beta^2}\left[\ln\left(\frac{2m_e c^2 W_0}{I^2}\beta^2\gamma^2\right) - \beta^2 - \delta\right]$$

where $I$ is the mean excitation energy, $W_0$ is the maximum energy transfer, $\delta$ is the density effect correction, which is parameterized in Ref. [8].

The separation power between two particle species A and B using $dE/dx$ measurement is defined in Ref. [9] as

$$S(A/B) = \frac{(dE/dx)_A - (dE/dx)_B}{\sigma_{A,B}}$$

where $\sigma_{A,B}$ is the average standard deviation of the measured $dE/dx$ for the particle species A and B. The separation power is calculated using the fitted curves in Fig. 16 with the $dE/dx$ resolution fixed at that of the minimum ionization. Fig. 17 shows the particle separation power as a function of the momentum for different particle species at 2150 V. The result for 2200 V is also presented for comparison. The separation power particularly for π and K in the low momentum region ($<1\,\mathrm{GeV}/c$) is most relevant for the BESIII drift chamber. The $3\sigma$ π/K separation is up to 735 MeV/$c$ at 2150 V and 715 MeV/$c$ at 2200 V as shown in the figure. The increase of the operating voltage degrades the separation power using $dE/dx$ measurement due to the gas gain saturation, but not very serious from 2150 to 2200 V.

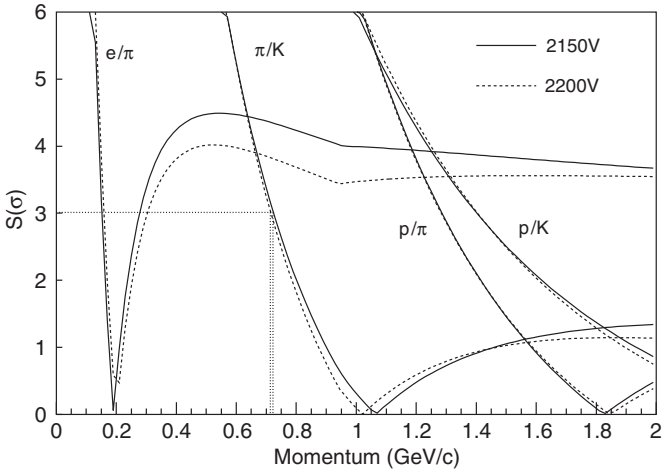


Fig. 17. The separation power as a function of the momentum.

### 3.4. Cell efficiency

The cell efficiency is obtained by the ratio of the number of times being fired to that of being passed through by the tracks, as shown in Fig. 18 for all layers at $B = 0$ and 1T. All layers have reasonably high efficiencies although those of the boundary layers are lower than that of other layers. The magnetic field has negligible impact on the efficiency except for the boundary layers.

Fig. 19 shows the dependence of the efficiency on the drift distance. The efficiency drops near the sense wire and cell edge due to the very non-isochronic charge collection which results in the smaller signal with slow rise time.

The efficiency averaged over the non-boundary layers in the 1T magnetic field is shown in Fig. 20 as a function of the operating voltage. The efficiency increases with the operating voltage until a plateau over 98% is reached at an operating voltage exceeding 2200 V. The BESIII drift chamber can in such a case operate with a high efficiency in a strong magnetic field of 1T.

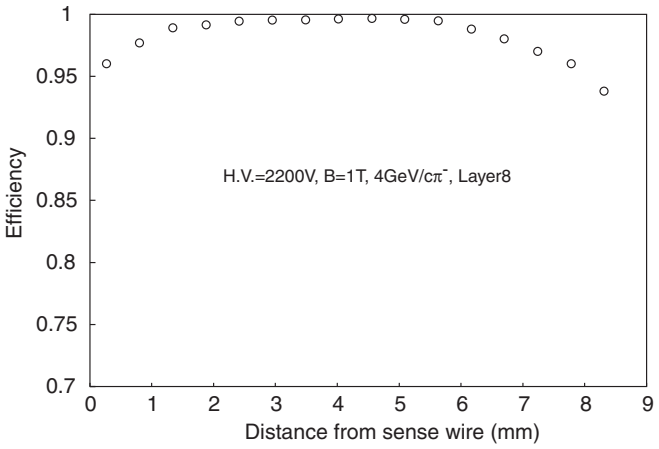


Fig. 19. Drift distance dependence of the efficiency.

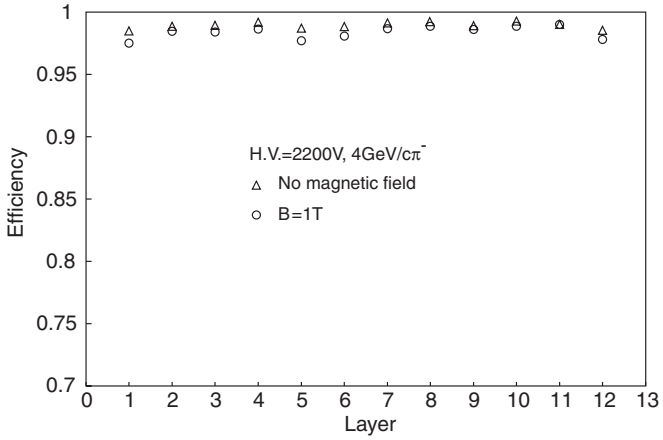


Fig. 18. Efficiencies for all layers.

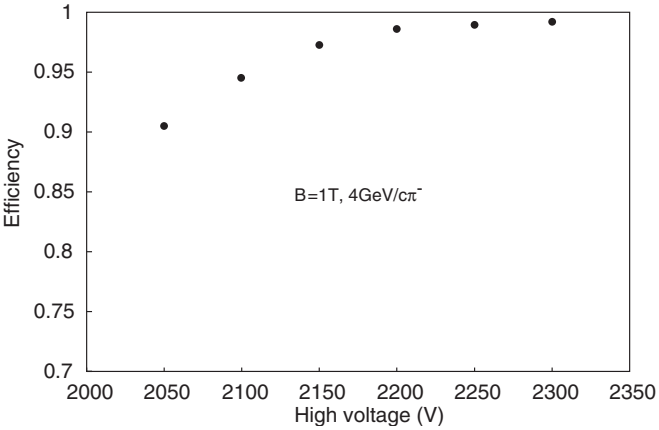


Fig. 20. Efficiency as a function of the operating voltage.

## 4. Conclusion

A beam test of a prototype of the BESIII drift chamber was performed in a 1T magnetic field. The test results show that the BESIII drift chamber can operate in a strong magnetic field with good performance.

For the operating voltage optimization of the BESIII drift chamber, the following factors should be taken into account: good spatial resolution, high cell efficiency, particle identification using $dE/dx$ measurement and low surface electric field for field wires to avoid the potential aging problem [10]. Based on these considerations and the test results, 2200 V is chosen as the optimized operating voltage for the drift chamber. At this voltage, the spatial resolution is better than 110 μm, the cell efficiency is over 98%, the $dE/dx$ resolution is better than 5% and the $\pi/K$ separation extends to 700 MeV/$c$, and the surface electric field of field wires is less than 20 kV/cm. The transverse momentum resolution is expected to reach 0.46%@1 GeV/$c$. These test beam results can verify the physics design of the BESIII drift chamber.

## Acknowledgements

We would like to thank Mr. Shoji Uno and his colleagues for their great support on the apparatus and instrument for the beam test and their essential help for the preparation of the test. We are also very grateful to Mr. Shoji Uno for his help in the DAQ tuning and very useful discussions and advices during the data taking. We also want to thank the KEK PS members for the use of the $\pi - 2$ beam line.

## References

[1] BESIII Collaboration, BESIII Preliminary Design Report, 2004.
[2] BEPCII Preliminary Design Report, 2002.
[3] L.H. Wu, et al., High Energy Phys. Nucl. Phys. 29 (2005) 476 (in Chinese).
[4] V. Cindro, et al., Nucl. Instr. and Meth. A 309 (1991) 411.
[5] D. Jeanne, et al., Nucl. Instr. and Meth. A 111 (1973) 287.
[6] W. Allison, J.H. Cobb, Ann. Rev. Nucl. Part. Sci. 30 (1980) 253.
[7] H. Messel, D.M. Ritson, Philos. Mag. 41 (1950) 1129.
[8] R.M. Sternheimer, R.F. Peierls, Phys. Rev. B 3 (1971) 3681.
[9] M. Hauschild, Nucl. Instr. and Meth. A 379 (1996) 436.
[10] J.A. Kadyk, Nucl. Instr. and Meth. A 300 (1991) 436.